Synergistic Engineering of Dendritic Ni-Cu-Co-P Electrocatalyst via Dynamic Hydrogen Bubble Template for Efficient and Durable Bifunctional Water Splitting

Ali Talebi[a], Ghasem Barati Darband*[a], Mostafa Mirjalili[a], Jinyang Li[b,c]

a- Materials and Metallurgical Engineering Department, Faculty of Engineering, Ferdowsi University of Mashhad, Mashhad 91775-1111, Iran

b- School of Chemistry, Key Laboratory of Advanced Technologies of Materials (Ministry of Education), Southwest Jiaotong University, Chengdu, 610031, China

c.Yibin Institute of Southwest Jiaotong University, Yibin 644000, China.

Corresponding author: E-mail: baratidarband@um.ac.ir

1. Experimental method

1.1. Synthesis of Ni-Cu-Co-P on NF

To synthesize the Ni-Cu-Co-P electrocatalyst, a NF substrate underwent a pretreatment process beginning with immersion in 96% C_2H_5OH, followed by treatment in 20% HCl. Subsequently, the substrate was rinsed thoroughly with deionized water and immersed in an electrodeposition bath formulated with 0.4 M $NiSO_4.6H_2O$, 0.04 M $CuSO_4.5H_2O$, and 0.4 M $CoSO_4.6H_2O$ as sources of Ni^{2+}, Cu^{2+}, and Co^{2+} ions, respectively. Furthermore, 0.02 M $NaH_2PO_2.H_2O$ was incorporated as a P precursor, enabling the release of P ions under reductive conditions for the in-situ formation of metal phosphide phases. To enhance the ionic conductivity and facilitate efficient ion transport in the electrolyte, 1 M NaCl was added. Additionally, to regulate the pH and maintain an acidic environment favorable for electrodeposition, 1 M H_2SO_4 was introduced. The deposition procedure was carried out galvanostatically at room temperature using a direct current (DC) power supply in a two-electrode cell containing 30 ml of the prepared bath. In this configuration, NF served as the cathode, while a Pt sheet functioned as the anode. Electrodeposition was performed under a constant current density of 2 $A.cm^{-2}$. To explore the influence of deposition time on the structural and electrocatalytic performance, a series of electrodes were fabricated at various durations (20, 50, 80, 100, and 120 seconds) under identical current conditions. After deposition, each electrode was rinsed with deionized water and air-dried. For clarity and consistency throughout the manuscript, a specific coding system was assigned to each sample (e.g., S-20 for 20 s deposition), as summarized in Table S1.

Table S1. Sample Designation and Labeling Scheme

Samples	Deposition time (s)
S-20	20
S-50	50
S-80	80
S-100	100
S-120	120

1.2. Material characterization

To investigate the surface morphology of the fabricated electrocatalyst coatings, field-emission scanning electron microscopy (FESEM; MIRA3, TESCAN) was employed. The elemental composition of the coatings was analyzed by energy-dispersive X-ray spectroscopy (EDS) using a VP 1450 system (LEO, Germany). Transmission electron microscopy (TEM) and high-resolution TEM (HRTEM) analyses were performed using a JEOL JEM-2100 instrument to elucidate the microstructure at higher spatial resolution. Elemental distribution and compositional information were further examined by scanning TEM (STEM) coupled with EDS. The phase structure and crystallographic characteristics of the samples were identified by X-ray diffraction (XRD) using an X'Pert MPD diffractometer with Cu Kα radiation (λ = 1.54178 Å), and the diffraction patterns were analyzed using HighScore Plus software. To evaluate the homogeneity of elemental

distribution within the synthesized electrocatalyst layers, elemental mapping was conducted on the optimal electrode. Fourier-transform infrared (FTIR) spectroscopy (AVATAR 370 FT-IR, Thermo Nicolet, USA) was utilized to gain deeper insight into chemical composition and vibrational modes associated with surface functional groups. In addition, X-ray photoelectron spectroscopy (XPS; Thermo Scientific ESCALAB 250Xi) was carried out to probe the surface elemental composition, chemical states, and phase-related surface features of the prepared samples.

1.3. Electrochemical measurements

All electrochemical tests in this study were conducted using a conventional three-electrode configuration. A Pt sheet served as the counter electrode, while an Ag/AgCl electrode was used as the reference. The working electrode consisted of the synthesized electrocatalysts. A 1.0 M KOH aqueous solution was used as the electrolyte for all measurements. The electrochemical experiments were performed at room temperature using a ZIVE potentiostat. To ensure consistency and comparability of results, all measured potentials were converted to the reversible hydrogen electrode (RHE) scale using Equation 1:

$$E_{(vs.\ RHE)} = E_{(vs.\ Ag/AgCl)} + 0.197 + 0.0591 \times pH \quad (1)$$

Moreover, to minimize the influence of solution resistance, potential drop (iR) compensation was applied, with the solution resistance values obtained via electrochemical impedance spectroscopy (EIS). The electrocatalytic activity of the synthesized electrodes toward the HER and OER was assessed by linear sweep voltammetry (LSV). For HER analysis, the potential window was set between –0.5 and –2.0 V vs. Ag/AgCl, while for OER, the range was 0 to +2.0 V vs. Ag/AgCl. All LSV measurements were carried out at a scan rate of 5 $mV.s^{-1}$. The Tafel slope was derived from the linear region of the LSV curves to evaluate the kinetics of hydrogen and oxygen evolution. To quantitatively estimate the electrochemically active surface area (ECSA), cyclic voltammetry (CV) was performed within the non-faradaic region. The electrodes were immersed in electrolyte solution until a stable open circuit potential (OCP) was achieved, followed by CV tests within ±50 mV around the OCP. The measurements were conducted at various scan rates: 10, 20, 30, 40, 50, 60, 70, 80, 90, and 100 $mV.s^{-1}$. For each scan rate, the average absolute values of anodic and cathodic current densities were calculated and plotted versus the scan rate. The slope of the resulting linear plot corresponds to the double-layer capacitance (C_{dl}). The ECSA was then calculated using a standard specific capacitance value. EIS was employed to further investigate the electrocatalytic behavior of the synthesized electrodes. Separate EIS measurements were conducted for HER and OER. For HER, impedance spectra were recorded in the frequency range of 100 kHz to 100 mHz at three different potentials: –1200, –1300, and –1400 mV vs. Ag/AgCl. Similarly, for OER, the measurements were carried out within the same frequency range at +600, +700, and +800 mV vs. Ag/AgCl. The impedance data was analyzed using Nyquist plots generated with ZMAN software, and key electrochemical parameters were extracted. To evaluate the long-term operational durability of the synthesized electrocatalysts under practical conditions, chronopotentiometry stability tests were conducted in alkaline media. For HER performance, the electrodes were tested at a constant current density of –100 mA cm^{-2} for 100 hours, and the variation in potential over time was monitored. A similar test was performed for OER at a constant current density of +100 mA cm^{-2} for 100 hours under the same electrolyte conditions. To study the superhydrophobic behavior of the electrode surfaces, dynamic surface resistance measurements, a subset of EIS analysis, were conducted. This test was performed for 600 seconds at a frequency of 1 Hz and a constant current density of –30 $mA.cm^{-2}$. Both the Ni-Cu-Co-P@NF electrode and a Pt

sheet were included as comparative samples. Wettability characteristics were further assessed through static water contact angle measurements using a contact angle goniometer (SCAM-S1, MehrTavNegar Alborz, Iran). The contact angle of a water droplet on the electrode surface was measured to determine its hydrophilic or hydrophobic nature. Furthermore, to evaluate the electrode surface's ability to release gas bubbles which plays a key role in enhancing water splitting (WS) efficiency and reducing bubble-induced resistance, the detachment behavior of bubbles was recorded using an optical camera (Dino-Lite AM132) for 20 seconds at a constant current density of –30 mA cm^{-2}. Finally, to verify the practical applicability of the synthesized electrocatalysts in an overall WS system, a two-electrode cell was assembled. The optimized HER electrode served as the cathode, and the optimized OER electrode functioned as the anode. The cell voltage was gradually increased, and the resulting current density was recorded. A plot of current density versus applied voltage was then generated, allowing for precise assessment of the overall WS performance of the combined electrodes.

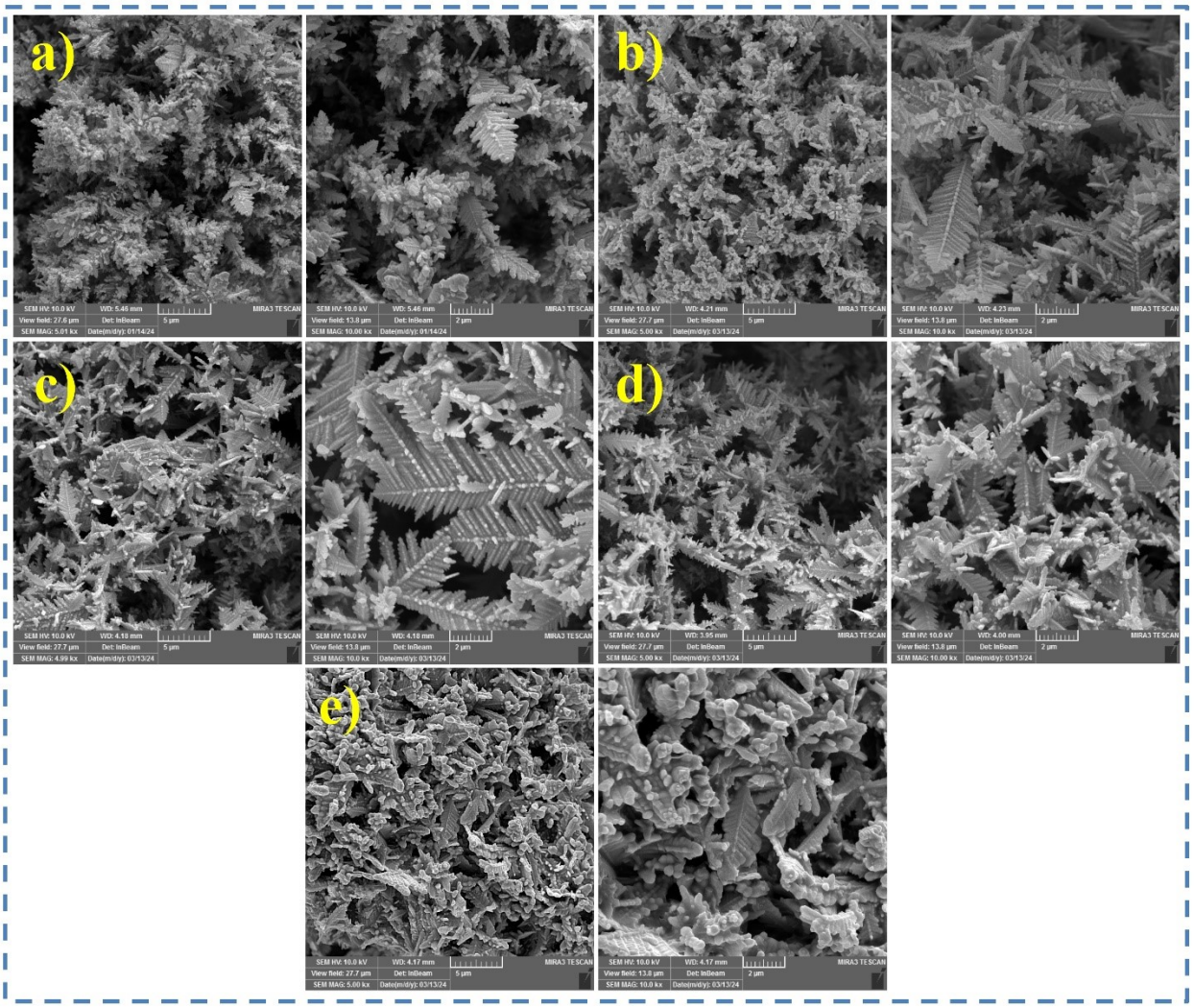

Fig. S1. FESEM images of the electrodeposited Ni-Cu-Co-P electrodes at different deposition times: a) S-20, b) S-50, c) S-80, d) S-100, and e) S-120.

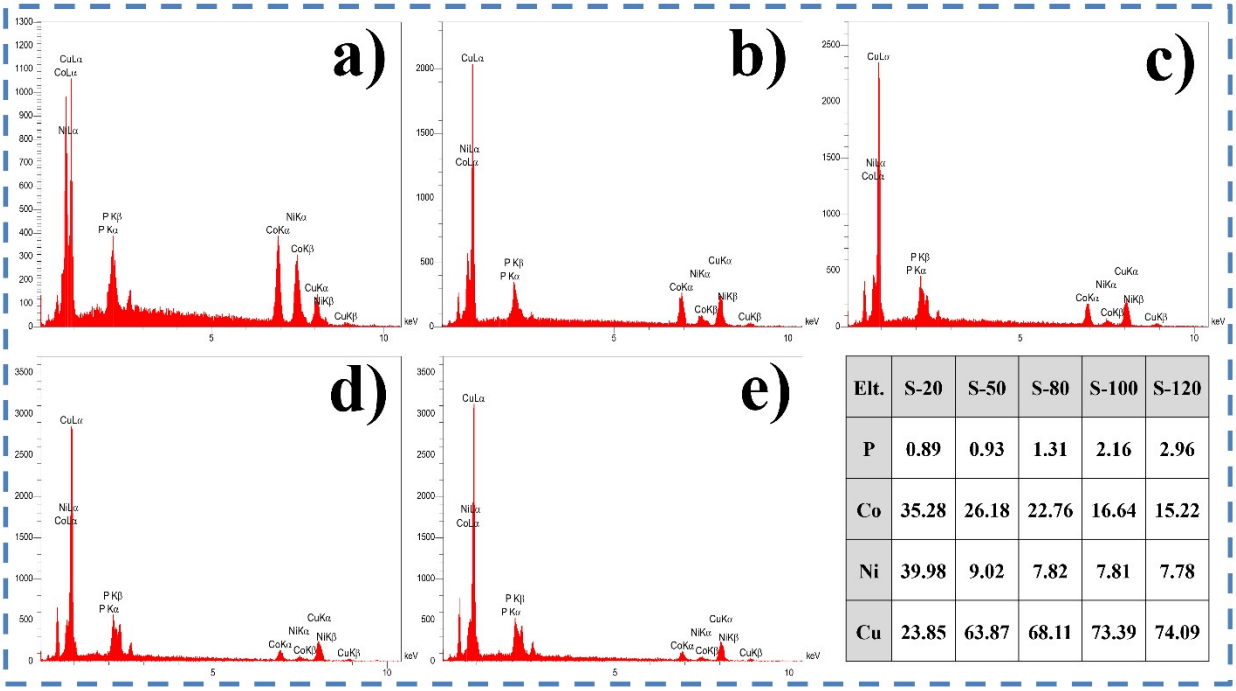

Elt.	S-20	S-50	S-80	S-100	S-120
P	0.89	0.93	1.31	2.16	2.96
Co	35.28	26.18	22.76	16.64	15.22
Ni	39.98	9.02	7.82	7.81	7.78
Cu	23.85	63.87	68.11	73.39	74.09

Fig. S2. EDS analysis of a) S-20, b) S-50, c) S-80, d) S-100, and e) S-120.

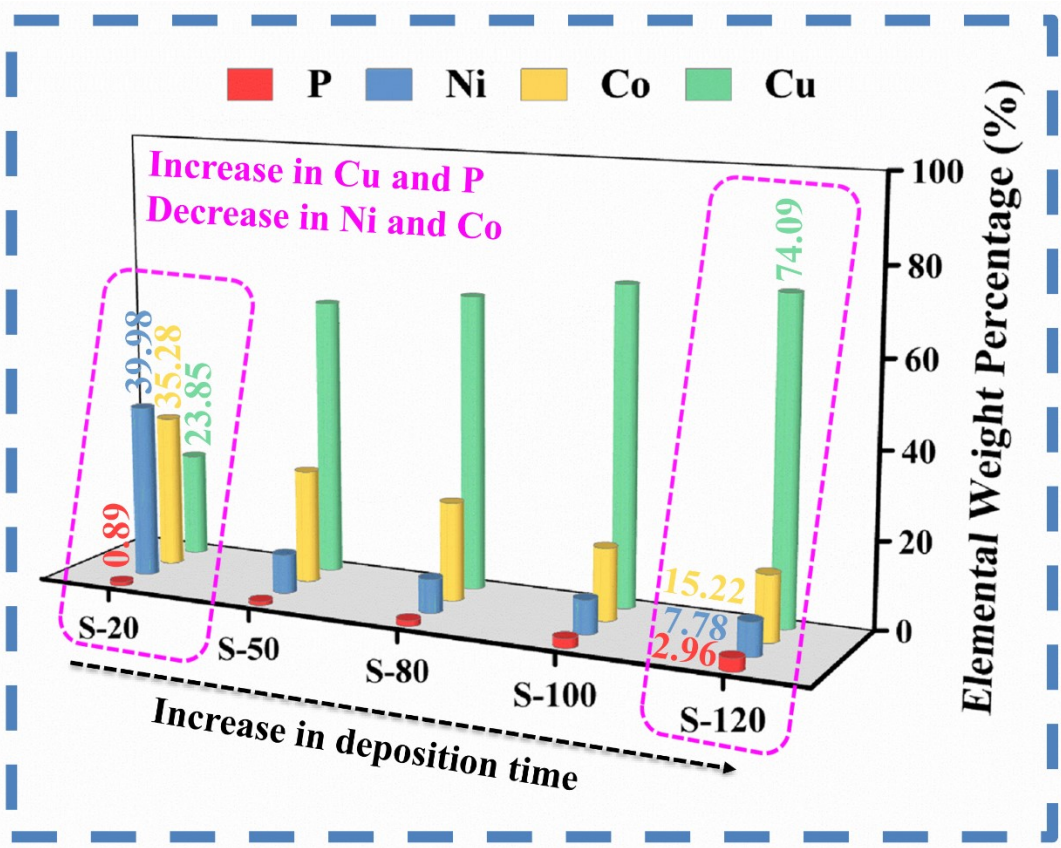

Fig. S3. Bar chart illustrating the EDS analysis results of the synthesized electrodes in this study.

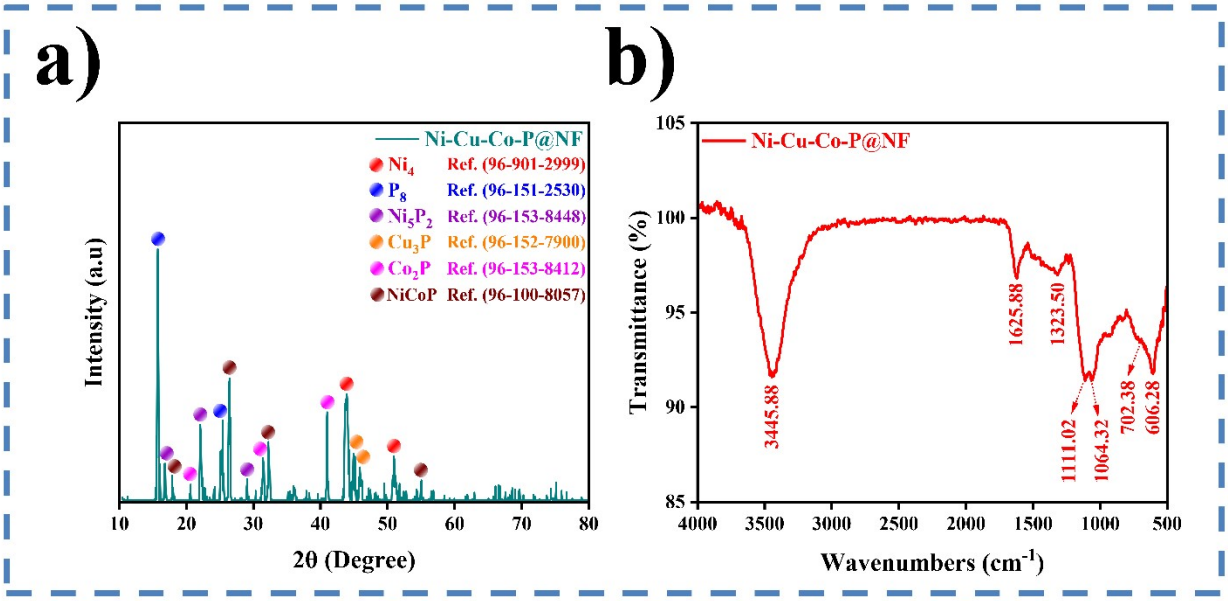

Fig. S4. a) XRD patterns of the Ni-Cu-Co-P electrode, and b) FTIR spectra of the Ni-Cu-Co-P sample.

Table S2. Comparative evaluation of the HER electrocatalytic performance of phosphide-based electrocatalysts in 1.0 M KOH solution.

Electrocatalyst	**η_{10} (mV)**	**b (mV.dec^{-1})**	**Reference**
Ni-Cu-Co-P@NF	81	69	This work
CoP/Co_2P@NC	198	82	[1]
Ni_2P@G	275	56.5	[2]
CoP-Co_2P	109	78.9	[3]
CoP (MoP)-$CoMoO_3$@CN	198	95	[4]
Ni_3S_2/Cu–NiCo LDH	156	84	[5]
CuCoP@Cu foil	231	86	[6]
NiCoFeP/C	149	89	[7]
CoNiP microspheres	148.5	52	[8]
CoP nanoframes	136	54.8	[9]
CoP/NiCoP	110	87.3	[10]
NC-$NiFeO_x$@NiFe-P	285	65	[11]
NiCoCu-P cage	210	72.5	[12]
$NiSe_2$–Ni_2P/NF	102	88	[13]
NiCo LDH/NiCoP/ Ni Foam	112	75.6	[14]

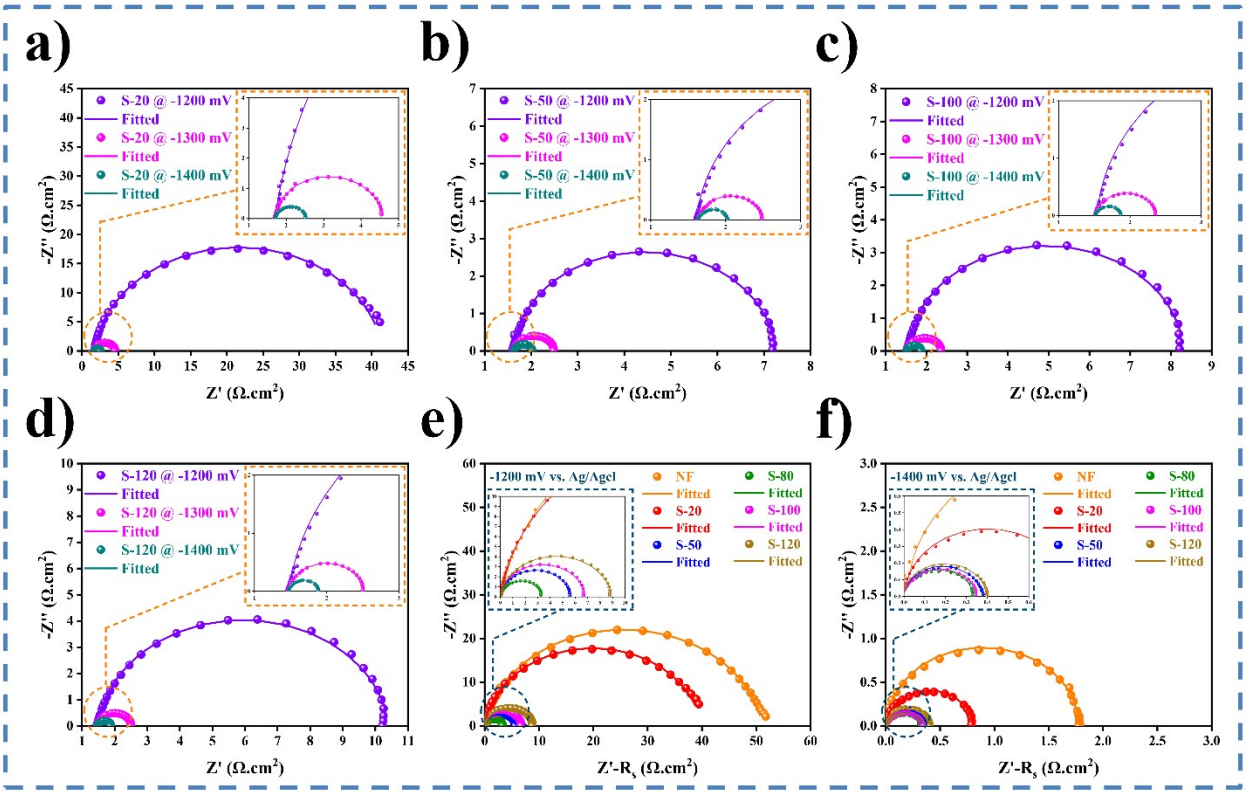

Fig. S5. Nyquist plots of a) S-20, b) S-50, c) S-100, and d) S-120 recorded at various overpotentials, and Nyquist plot of Ni-Cu-Co-P@NF electrode deposited at an overpotential of e) -1200 mV, and f) -1400 mV.

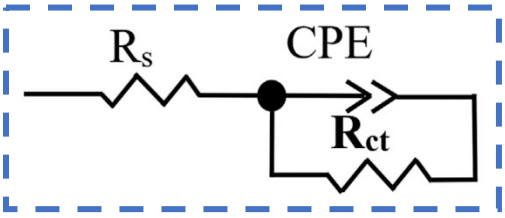

Fig. S6. A suitable EEC model enabling accurate simulation of the system's electrochemical response.

Table S3. Fitted EIS parameters for NF and the synthesized electrodes in this study.

Electrode	η (mV)	R_s (Ω.cm^{-2})	R_{ct} (Ω.cm^{-2})	CPE (Fs^{n-1}.cm^{-2})	n
	-1200	1.396	52.249	0.00060	0.902
NF	-1300	1.501	5.553	0.00032	0.956
	-1400	1.611	1.795	0.00026	0.982
	-1200	1.702	39.849	0.00461	0.928
S-20	-1300	1.712	2.859	0.00242	0.929
	-1400	1.724	0.808	0.00168	0.941
	-1200	1.616	5.628	0.01040	0.960
S-50	-1300	1.634	0.857	0.00714	0.957
	-1400	1.643	0.377	0.00531	0.974
	-1200	1.593	3.330	0.01683	0.961
S-80	-1300	1.582	0.684	0.01211	0.958
	-1400	1.581	0.334	0.00875	0.975
	-1200	1.541	6.771	0.01356	0.966
S-100	-1300	1.518	0.845	0.00974	0.953
	-1400	1.523	0.348	0.00695	0.971
	-1200	1.478	8.932	0.00938	0.936
S-120	-1300	1.475	1.034	0.00580	0.955
	-1400	1.484	0.399	0.00372	0.993

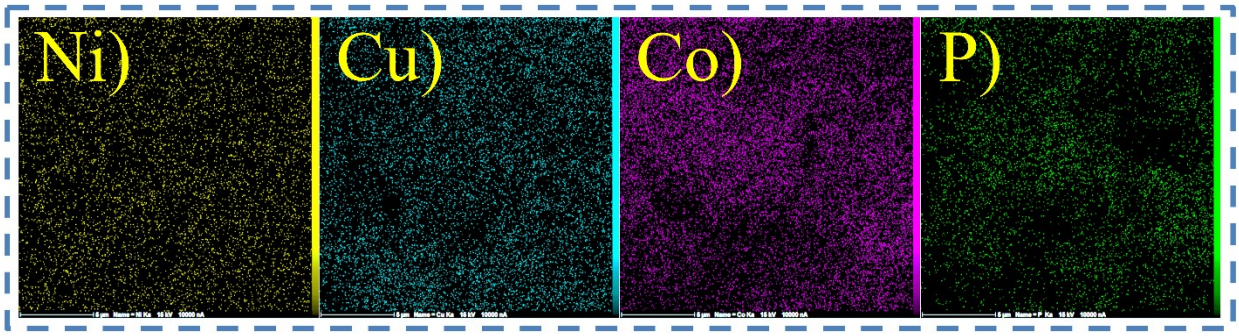

Fig. S7. Elemental mapping analysis of S-80 after stability test.

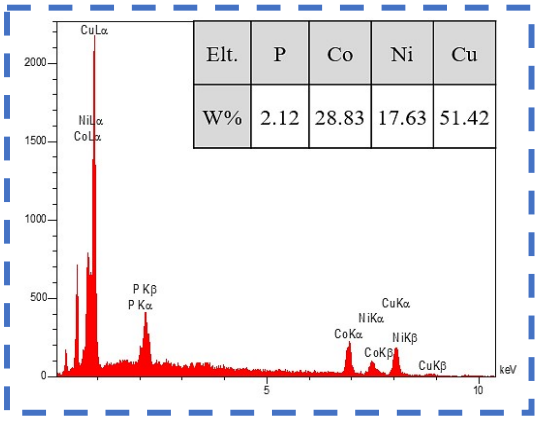

Fig. S8. EDS analysis of S-80 after stability test.

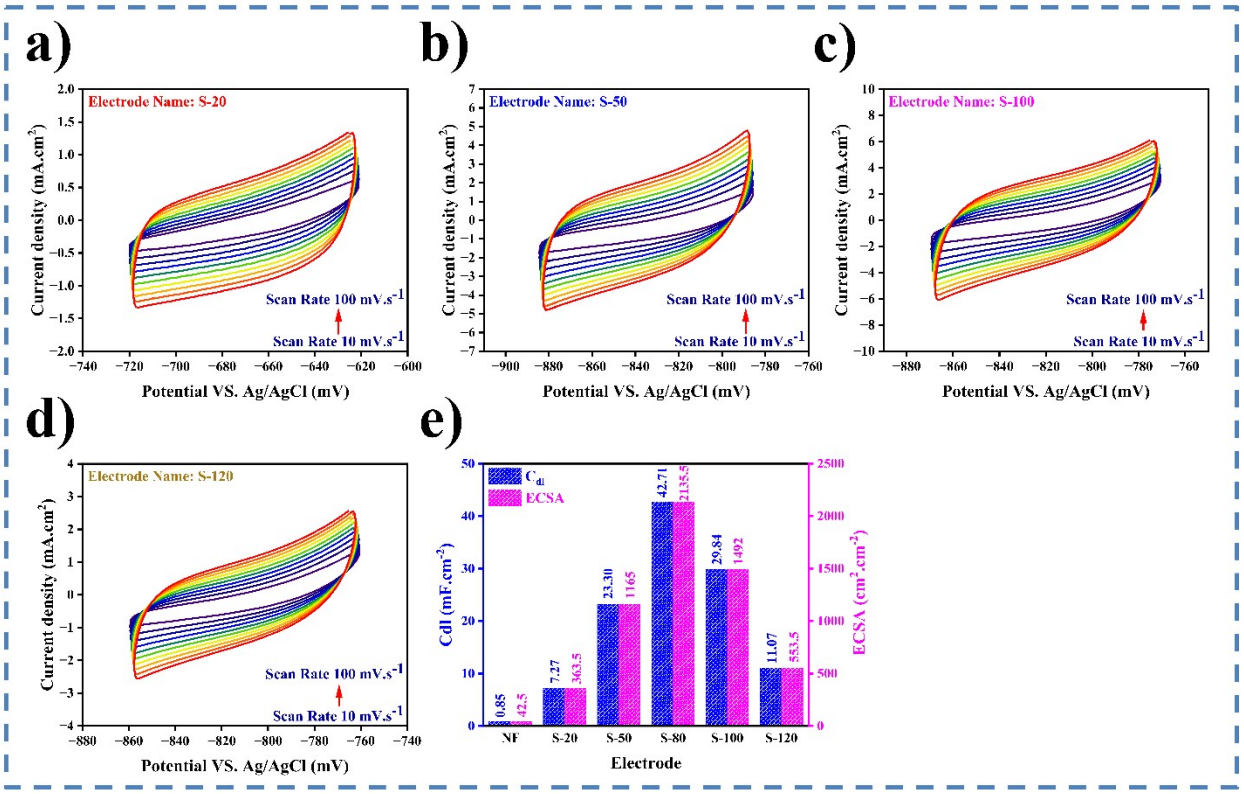

Fig. S9. CV curves recorded at various scan rates in the non-faradaic region for electrodes a) S-20, b) S-50, c) S-100, d) S-120, and e) C_{dl}, and ECSA plots for better comparison of all samples.

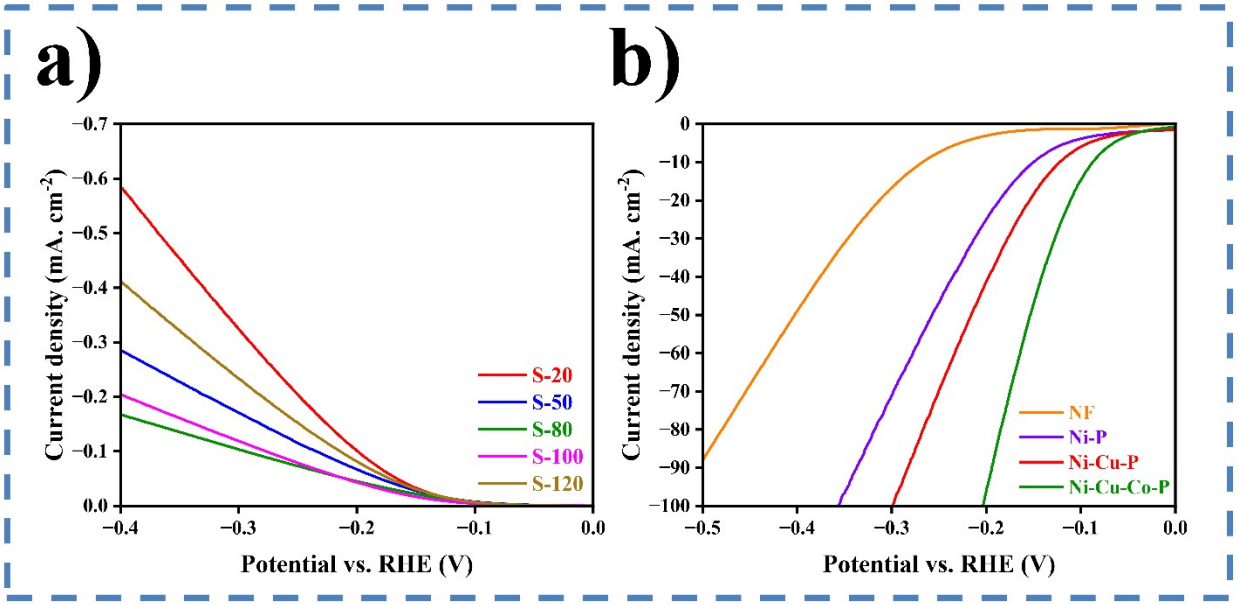

Fig. S10. a) ECSA-normalized current densities curves, b) LSV curves of control electrodes, confirming improved HER activity with multimetallic integration.

Table S4. Comparative evaluation of the OER electrocatalytic performance of phosphide-based electrocatalysts in 1.0 M KOH solution.

Electrocatalyst	η_{10} (mV)	b (mV.dec^{-1})	Reference
Ni-Cu-Co-P@NF	248	64	This work
Co_xP/N-doped C	380	68.1	[15]
CoP-Co_2P@PC/PG	272	66	[16]
$NiCo_xP$@NiCo- LDH	269	97	[17]
$CoNiP_x$@$FeCoP_x$/C@$CoNiP_x$	298	74.5	[18]
Ni_5P_4@NiOOH	273	62	[19]
Cu_3P–Co_2P	334	132	[20]
C-CoP	323	71.1	[21]
NiCoP@Cu_3P	309	42	[22]
CoP nanoframes	323	49.6	[9]
Ru-Ni-Co-P/NC	318	84	[23]
CuP_2/$Ni_{1-x}Cu_x$–P@g-C_3N_4	280	66	[24]
$Ni_{59}Cu_{19}P_9$	307	42.5	[25]
CoP/NiCoP	310.7	104.5	[10]
Co-Ni-P	277	63.6	[26]

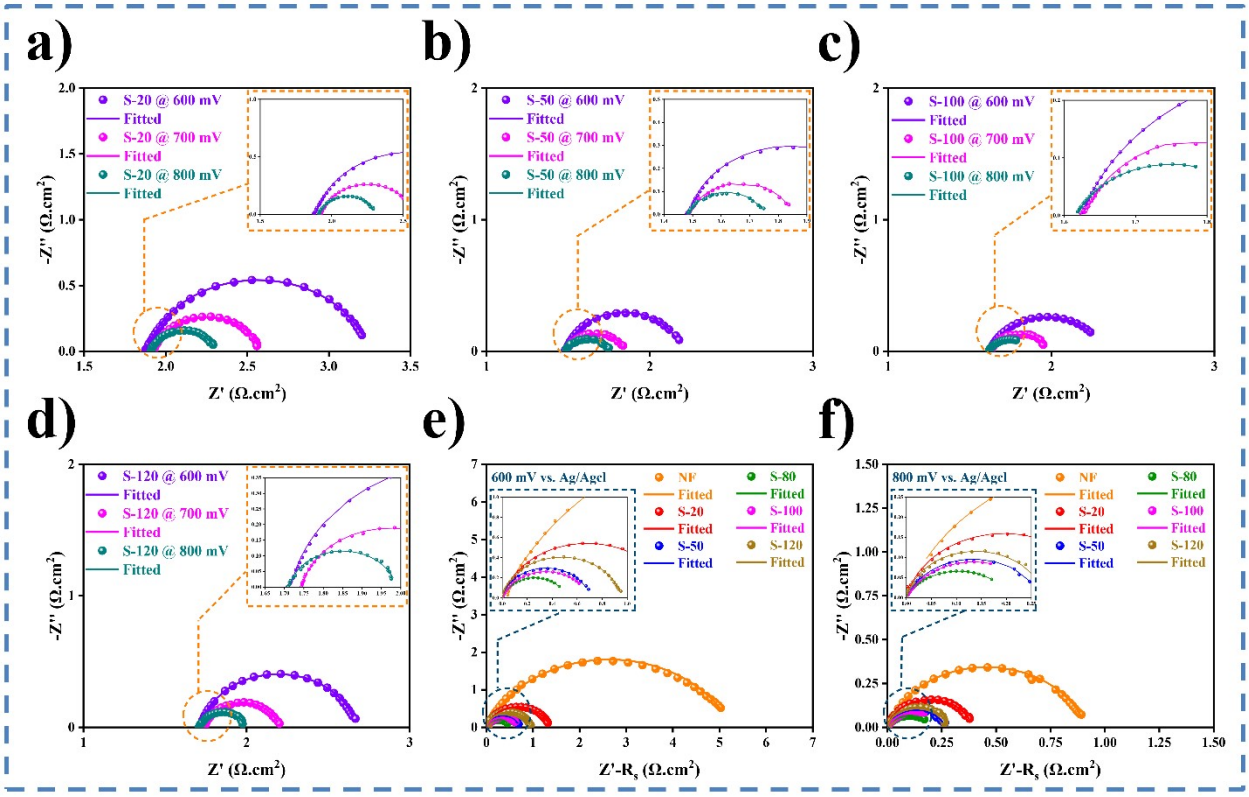

Fig. S11. Nyquist plots of a) S-20, b) S-50, c) S-100, and d) S-120 recorded at various overpotentials, and Nyquist plot of Ni-Cu-Co-P@NF electrode deposited at an overpotential of e) 600 mV, and f) 800 mV.

Table S5. Fitted EIS parameters for NF and the synthesized electrodes in this study.

Electrode	η (mV)	R_s ($\Omega.cm^{-2}$)	R_{ct} ($\Omega.cm^{-2}$)	CPE ($Fs^{n-1}.cm^{-2}$)	n
	600	1.744	5.269	0.00725	0.766
NF	700	1.805	1.998	0.00466	0.813
	800	1.845	0.915	0.00399	0.820
	600	1.885	1.359	0.11013	0.858
S-20	700	1.928	0.649	0.08591	0.864
	800	1.912	0.392	0.06838	0.870
	600	1.489	0.706	0.33319	0.890
S-50	700	1.488	0.362	0.37386	0.819
	800	1.484	0.269	0.39711	0.790
	600	1.475	0.520	0.78290	0.837
S-80	700	1.479	0.282	0.82615	0.794
	800	1.476	0.214	0.98138	0.702
	600	1.624	0.698	0.55220	0.817
S-100	700	1.630	0.349	0.55486	0.836
	800	1.616	0.268	0.65993	0.746
	600	1.717	0.954	0.12818	0.897
S-120	700	1.744	0.456	0.12288	0.879
	800	1.712	0.277	0.11697	0.885

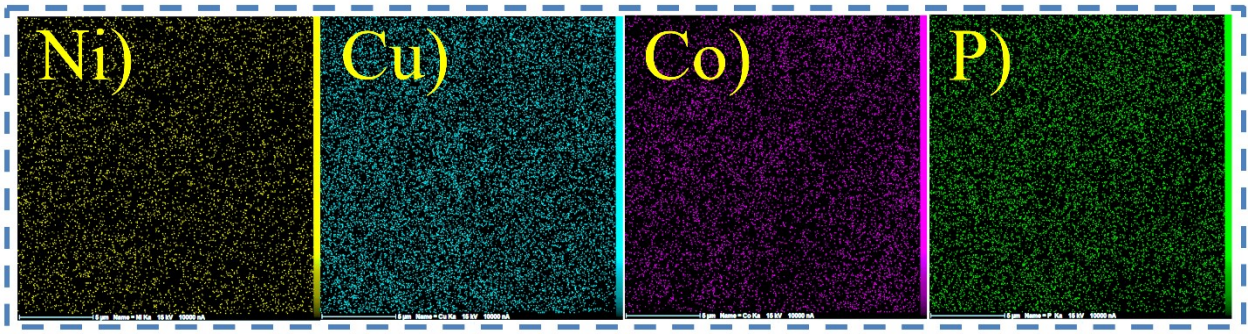

Fig. S12. Elemental mapping analysis of S-80 after stability test.

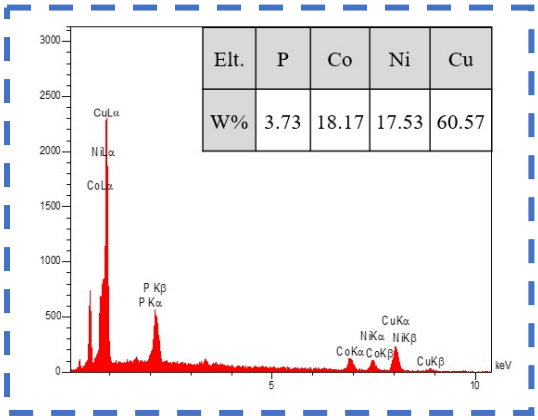

Fig. S13. EDS analysis of S-80 after stability test.

Table S6. Comparison of cell voltage at 10 $mA.cm^{-2}$ for this work with previously reported electrocatalysts in 1.0 M KOH solution.

Electrocatalyst	η_{10} (mV)	Reference
Ni-Cu-Co-P@NF	1.56	This work
Ni_2P@NC	1.67	[27]
Co/CoP	1.68	[28]
Ni-Co-P hollow nanobricks	1.62	[29]
CoP@a-CoO_x	1.66	[30]
$NiCo_2Px$/CNT	1.61	[31]
Co_xP/N-doped C	1.71	[15]
Ni_2P-NPCM	1.62	[32]
NiCoFeP/C	1.60	[7]
Co-P@PC	1.60	[33]
Cu-CoP NAs/CP	1.72	[34]
Ni–Co–P/GS	1.58	[35]
Co-Ni-P	1.64	[26]
CoP-Co_2P	1.60	[3]
$RhP_x/CoNiP_4O_{12}$	1.57	[36]
A-NiCoP	1.64	[37]
MnO_x/NiCoP/NF	1.59	[38]
CoP/NiCoP	1.63	[10]
NiCoP/FeNiCoP	1.58	[39]
Co_3O_4/P–C@NiFeP	1.67	[40]
$Ni_{0.3}Co_2Fe$–P	1.61	[41]
CeCoFeP@MXene	1.63	[42]
Co_2P/MnP@C–CNFs	1.58	[43]

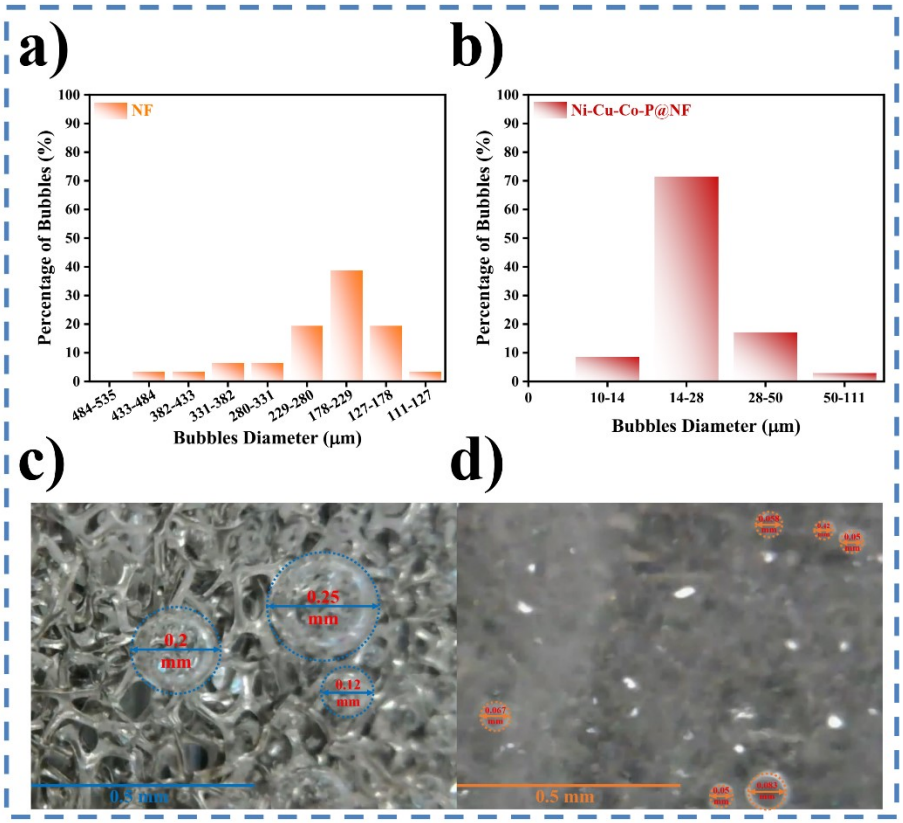

Fig. S14. Bubble-size analysis during HER on (a,c) bare NF and (b,d) Ni–Cu–Co–P@NF: (a,b) bubble diameter distributions from 10× optical images and (c,d) representative micrographs, showing significantly smaller and more uniform bubbles on the coated electrode compared with NF.

References

[1] X. Lv, J. Ren, Y. Wang, Y. Liu, and Z.-Y. Yuan, "Well-defined phase-controlled cobalt phosphide nanoparticles encapsulated in nitrogen-doped graphitized carbon shell with enhanced electrocatalytic activity for hydrogen evolution reaction at all-pH," *ACS Sustainable Chemistry & Engineering,* vol. 7, no. 9, pp. 8993-9001, 2019.

[2] H. Mou *et al.*, "A facile and controllable, deep eutectic solvent aided strategy for the synthesis of graphene encapsulated metal phosphides for enhanced electrocatalytic overall water splitting," *Journal of Materials Chemistry A,* vol. 7, no. 22, pp. 13455-13459, 2019.

[3] L. Chen, J.-T. Ren, and Z.-Y. Yuan, "Interface engineering for boosting electrocatalytic performance of CoP-Co2P polymorphs for all-pH hydrogen evolution reaction and alkaline overall water splitting," *Science China Materials,* vol. 65, no. 9, pp. 2433-2444, 2022.

[4] L. Yu *et al.*, "Cobalt/molybdenum phosphide and oxide heterostructures encapsulated in N-doped carbon nanocomposite for overall water splitting in alkaline media," *ACS Applied Materials & Interfaces,* vol. 11, no. 7, pp. 6890-6899, 2019.

[5] L. Jia *et al.*, "Ni_3S_2/Cu–NiCo LDH heterostructure nanosheet arrays on Ni foam for electrocatalytic overall water splitting," 2021.

[6] R. N. Wasalathanthri, S. Jeffrey, R. A. Awni, K. Sun, and D. M. Giolando, "Electrodeposited copper–cobalt–phosphide: a stable bifunctional catalyst for both hydrogen and oxygen evolution reactions," *ACS Sustainable Chemistry & Engineering,* vol. 7, no. 3, pp. 3092-3100, 2018.

[7] X. Wei *et al.*, "Carbon-incorporated porous honeycomb NiCoFe phosphide nanospheres derived from a MOF precursor for overall water splitting," *Chemical Communications,* vol. 55, no. 73, pp. 10896-10899, 2019.

[8] Y. Du *et al.*, "A self-templating method for metal–organic frameworks to construct multi-shelled bimetallic phosphide hollow microspheres as highly efficient electrocatalysts for hydrogen evolution reaction," *Journal of Materials Chemistry A,* vol. 7, no. 14, pp. 8602-8608, 2019.

[9] L. Ji, J. Wang, X. Teng, T. J. Meyer, and Z. Chen, "CoP nanoframes as bifunctional electrocatalysts for efficient overall water splitting," *ACS Catalysis,* vol. 10, no. 1, pp. 412-419, 2019.

[10] X. Fu *et al.*, "Cobalt phosphide/nickel–cobalt phosphide heterostructured hollow nanoflowers for high-performance supercapacitor and overall water splitting," *Journal of Colloid and Interface Science,* vol. 653, pp. 1272-1282, 2024.

[11] H.-b. Zheng, H.-h. Chen, Y.-l. Wang, P.-z. Gao, X.-p. Liu, and E. V. Rebrov, "Fabrication of magnetic superstructure NiFe2O4@ MOF-74 and its derivative for electrocatalytic hydrogen evolution with AC magnetic field," *ACS Applied Materials & Interfaces,* vol. 12, no. 41, pp. 45987-45996, 2020.

[12] Z. Rahmati, M. Roushani, and H. Hosseini, "Three-dimensional cage based on porous Ni–Co–Cu phosphide as efficient and stable bifunctional electrocatalysts for overall water splitting," *International Journal of Hydrogen Energy,* vol. 62, pp. 859-866, 2024.

[13] P. Wang *et al.*, "Coupling NiSe2-Ni2P heterostructure nanowrinkles for highly efficient overall water splitting," *Journal of Catalysis,* vol. 377, pp. 600-608, 2019.

[14] L. Zhang, J. Peng, Y. Yuan, W. Zhang, and K. Peng, "Bifunctional heterostructure NiCo-layered double hydroxide nanosheets/NiCoP nanotubes/Ni foam for overall water splitting," *Applied Surface Science,* vol. 557, p. 149831, 2021.

[15] J.-S. Li *et al.*, "Polydopamine-assisted construction of cobalt phosphide encapsulated in N-doped carbon porous polyhedrons for enhanced overall water splitting," *Carbon,* vol. 145, pp. 694-700, 2019.
[16] S. C. Shit, I. Mondal, S. Pendem, L. Bai, J. Y. Park, and J. Mondal, "MOF-derived bifunctional iron oxide and iron phosphide nanoarchitecture photoelectrode for neutral water splitting," *ChemElectroChem,* vol. 5, no. 19, pp. 2842-2849, 2018.
[17] Y. Zhang, X. Wu, G. Fu, F. Si, X.-Z. Fu, and J.-L. Luo, "NiFexP@ NiCo-LDH nanoarray bifunctional electrocatalysts for coupling of methanol oxidation and hydrogen production," *International Journal of Hydrogen Energy,* vol. 47, no. 39, pp. 17150-17160, 2022.
[18] J. Shi *et al.*, "A general strategy for synthesis of binary transition metal phosphides hollow sandwich heterostructures," *Small,* vol. 19, no. 30, p. 2302906, 2023.
[19] T. Wang *et al.*, "Unlocking the synergy of interface and oxygen vacancy by core-shell nickel phosphide@ oxyhydroxide nanosheets arrays for accelerating alkaline oxygen evolution kinetics," *Chemical Engineering Journal,* vol. 425, p. 131491, 2021.
[20] L. Liu *et al.*, "Quasi-layer Co 2 P-polarized Cu 3 P nanocomposites with enhanced intrinsic interfacial charge transfer for efficient overall water splitting," *Nanoscale,* vol. 11, no. 13, pp. 6394-6400, 2019.
[21] W. Li *et al.*, "C-CoP hollow microporous nanocages based on phosphating regulation: a high-performance bifunctional electrocatalyst for overall water splitting," *Nanoscale,* vol. 11, no. 36, pp. 17084-17092, 2019.
[22] X. Ma, Y. Chang, Z. Zhang, and J. Tang, "Forest-like NiCoP@ Cu 3 P supported on copper foam as a bifunctional catalyst for efficient water splitting," *Journal of Materials Chemistry A,* vol. 6, no. 5, pp. 2100-2106, 2018.
[23] D. Wang *et al.*, "Multisite engineering towards atomically dispersed Ru on Ni-Co-P composite with N-doped carbon matrix for robust water oxidation," *Journal of Electroanalytical Chemistry,* vol. 924, p. 116875, 2022.
[24] K. K. Mandari, N. Son, S. Pandey, and M. Kang, "Highly efficient ternary CuP2/Ni1−xCux–P@ g-C3N4 nanostructure for improved hydrogen and oxygen evolution reactions," *International Journal of Hydrogen Energy,* vol. 48, no. 45, pp. 17000-17013, 2023.
[25] B. K. Kim, S.-K. Kim, S. K. Cho, and J. J. Kim, "Enhanced catalytic activity of electrodeposited Ni-Cu-P toward oxygen evolution reaction," *Applied Catalysis B: Environmental,* vol. 237, pp. 409-415, 2018.
[26] L. Chai, S. Liu, S. Pei, and C. Wang, "Electrodeposited amorphous cobalt-nickel-phosphide-derived films as catalysts for electrochemical overall water splitting," *Chemical Engineering Journal,* vol. 420, p. 129686, 2021.
[27] X. Xiao *et al.*, "Engineering NiS/Ni2P heterostructures for efficient electrocatalytic water splitting," *ACS Applied Materials & Interfaces,* vol. 10, no. 5, pp. 4689-4696, 2018.
[28] Y. Hao, Y. Xu, W. Liu, and X. Sun, "Co/CoP embedded in a hairy nitrogen-doped carbon polyhedron as an advanced tri-functional electrocatalyst," *Materials Horizons,* vol. 5, no. 1, pp. 108-115, 2018.
[29] E. Hu, Y. Feng, J. Nai, D. Zhao, Y. Hu, and X. W. D. Lou, "Construction of hierarchical Ni–Co–P hollow nanobricks with oriented nanosheets for efficient overall water splitting," *Energy & Environmental Science,* vol. 11, no. 4, pp. 872-880, 2018.
[30] J. Yu *et al.*, "Bifunctionality from synergy: CoP nanoparticles embedded in amorphous CoOx nanoplates with heterostructures for highly efficient water electrolysis," *Advanced Science,* vol. 5, no. 9, p. 1800514, 2018.

[31] C. Huang, T. Ouyang, Y. Zou, N. Li, and Z.-Q. Liu, "Ultrathin NiCo 2 P x nanosheets strongly coupled with CNTs as efficient and robust electrocatalysts for overall water splitting," *Journal of Materials Chemistry A,* vol. 6, no. 17, pp. 7420-7427, 2018.
[32] L. Yan *et al.*, "One-step and scalable synthesis of Ni2P nanocrystals encapsulated in N, P-codoped hierarchically porous carbon matrix using a bipyridine and phosphonate linked nickel metal–organic framework as highly efficient electrocatalysts for overall water splitting," *Electrochimica Acta,* vol. 297, pp. 755-766, 2019.
[33] J. Wu, D. Wang, S. Wan, H. Liu, C. Wang, and X. Wang, "An efficient cobalt phosphide electrocatalyst derived from cobalt phosphonate complex for all-pH hydrogen evolution reaction and overall water splitting in alkaline solution," *Small,* vol. 16, no. 15, p. 1900550, 2020.
[34] L. Yan, B. Zhang, J. Zhu, Y. Li, P. Tsiakaras, and P. K. Shen, "Electronic modulation of cobalt phosphide nanosheet arrays via copper doping for highly efficient neutral-pH overall water splitting," *Applied Catalysis B: Environmental,* vol. 265, p. 118555, 2020.
[35] A. Meng *et al.*, "Bimetal nickel–cobalt phosphide directly grown on commercial graphite substrate by the one-step electrodeposition as efficient electrocatalytic electrode," *Progress in Natural Science: Materials International,* vol. 30, no. 4, pp. 461-468, 2020.
[36] B. Guo *et al.*, "Noble metal phosphides supported on CoNi metaphosphate for efficient overall water splitting," *ACS Applied Materials & Interfaces,* vol. 16, no. 7, pp. 8939-8948, 2024.
[37] W. Hou *et al.*, "Preparation and overall water-splitting performance study of amorphous nickel-copper-phosphide," *Journal of Alloys and Compounds,* vol. 1002, p. 175314, 2024.
[38] Z. Zhang, L. Han, and K. Tao, "MnO x-decorated MOF-derived nickel–cobalt bimetallic phosphide nanosheet arrays for overall water splitting," *Dalton Transactions,* vol. 53, no. 4, pp. 1757-1765, 2024.
[39] P. Gao *et al.*, "Construction of unique NiCoP/FeNiCoP hollow heterostructured ellipsoids with modulated electronic structure for enhanced overall water splitting," *Journal of Colloid and Interface Science,* 2024.
[40] J. Li, R. Chai, X. Sang, and D. Wang, "Co-Gallate MOF-Derived Transition Metal Oxide/Phosphide Heterostructure for Efficient Overall Water Splitting," *Langmuir,* 2025.
[41] L. Yang and L. Li, "Synthesis of uniformly dispersed NiCoFe trimetallic phosphide for efficient overall water splitting," *Journal of Physics and Chemistry of Solids,* vol. 207, p. 112926, 2025.
[42] Y.-H. Pan *et al.*, "Reconstructed vanadium carbide MXene supported cerium based trimetallic phosphide as an efficient electrocatalyst for alkaline water splitting," *Chemical Engineering Journal,* p. 163888, 2025.
[43] X. Liu *et al.*, "Co2P/MnP Nanoarrays Loaded on Coal-Based Carbon Nanofibers Serve as Effective Bifunctional Catalysts for Overall Water Splitting," *ACS Applied Nano Materials,* 2025.